Substorm Activity as a Driver of Energetic Pulsating Aurora

Riley Troyer[1,1,1,1], ALLISON JAYNES[1,1,1,1], Stephen Kaeppler[2,2,2,2], Roger Varney[3,3], Ashton Reimer[3,3,3,3], Sarah Jones[4,4,4,4], and Roger Varney[5,5]

[1]University of Iowa
[2]Clemson University
[3]Formerly of SRI International
[4]Formerly of NASA Goddard
[5]Department of Atmospheric and Oceanic Sciences University of California, Los Angeles

May 23, 2023

Abstract

Pulsating aurora are common diffuse-like aurora. Studies have suggested that they contain higher energy particles than other types and are possibly linked to substorm activity. There has yet to be a quantitative statistical study of pulsating aurora energy content. We analyzed the inverted energy content from 53 events using the Poker Flat Incoherent Scatter Radar. We compared this to magnetic local time (MLT), AE index, and temporal proximity to substorm onset. There was a slight trend in MLT, but a much stronger one in relation to both substorm onset and AE index. For higher AE and closer to onset the total energy flux and flux above 30 keV increased. In addition, this higher energy remained enhanced for an hour after substorm onset. Our results confirm the high energy nature of pulsating aurora, demonstrate the connection to substorms, and imply their importance to coupling between the magnetosphere and atmosphere.

Substorm Activity as a Driver of Energetic Pulsating Aurora

R. N. Troyer [1], A. N. Jaynes [1], S. L. Jones [2], S. R. Kaeppler [3], R. H. Varney [4], A. S. Reimer [5]

[1]Department of Physics and Astronomy, University of Iowa
[2]Formerly of NASA Goddard Space Flight Center
[3]Clemson University
[4]Department of Atmospheric and Oceanic Sciences, University of California, Los Angeles
[5]Formerly of SRI International

Key Points:

- We analyzed the inverted energy content for 53 pulsating aurora events and found a close relationship to substorm onset and AE index.
- The average total energy flux and hardness increase closer to substorm onset and for higher AE indices.
- The energy hardness remains enhanced for approximately 1 hour after substorm onset.

Corresponding author: Riley Troyer, `riley-troyer@uiowa.edu`

Abstract

Pulsating aurora are common diffuse-like aurora. Studies have suggested that they contain higher energy particles than other types and are possibly linked to substorm activity. There has yet to be a quantitative statistical study of pulsating aurora energy content. We analyzed the inverted energy content from 53 events using the Poker Flat Incoherent Scatter Radar. We compared this to magnetic local time (MLT), AE index, and temporal proximity to substorm onset. There was a slight trend in MLT, but a much stronger one in relation to both substorm onset and AE index. For higher AE and closer to onset the total energy flux and flux above 30 keV increased. In addition, this higher energy remained enhanced for an hour after substorm onset. Our results confirm the high energy nature of pulsating aurora, demonstrate the connection to substorms, and imply their importance to coupling between the magnetosphere and atmosphere.

Plain Language Summary

Not all aurora (northern lights) are bright and defined curtains of light. Diffuse aurora are more modest. Barely visible to the naked eye, they spread across large portions of the night sky and can be easily overlooked. Pulsating aurora are a common and more playful type of diffuse aurora. In one of these displays, widely varying patches of aurora blink on and off with with periods ranging up to 20 seconds. While they aren't as bright, it has been suspected that the electrons which cause pulsating aurora are much more energetic than other types of aurora. Since energetic electrons move faster and thus can reach further into the atmosphere, it is possible that pulsating aurora may affect terrestrial climate. To study this, we first need a better understanding of pulsating aurora energies and how they can vary. In this study, we looked at the energy of 53 pulsating aurora events. In doing so, we confirmed that the energy of pulsating aurora is much higher than other types of aurora. We also found that the most energetic aurora happen close in time to a magnetic disturbance known as a substorm and that a stronger disturbance leads to higher energies.

1 Introduction

Pulsating aurora are a stark contrast to the bright curtains of discrete aurora that often precede them. Diffuse and barely visible to the naked eye, this type of aurora is

most often observed a few hours after magnetic midnight (e.g., Oguti et al., 1981; Jones et al., 2011). Often staying out for hours, pulsating aurora can cover large portions of the sky and in some cases expand over entire sections of the auroral region (Jones et al., 2013). Using SuperDarn and imager data, E. Bland et al. (2021) found that around half of pulsating aurora events extend between 4-5 hours of magnetic local time and between 62° to 70° in magnetic latitude. Over this area, auroral patches blink on and off with periods ranging up to around 20 seconds (e.g., Davis, 1978; Lessard, 2012). Adding to the auroral display, individual patches can be remarkably varied with differing periods, shapes, and sizes typically between 10s to 100s of kilometers (Johnstone, 1978; Lessard, 2012). Figure 1 panels A1-A3 shows a typical example of pulsating aurora that occurred on October 13, 2016 over the Poker Flat Research Range. The red oval highlights a patch that turns on and off during the three images.

Numerous studies have shown that the electrons responsible for pulsating aurora originate in the equatorial region of the outer Van Allen radiation belt. These electrons are pitch-angle scattered into the upper-atmosphere through wave-particle interactions, most likely with lower-band chorus waves (Nishimura et al., 2010, 2011; Jaynes et al., 2013; Kasahara et al., 2018; Hosokawa et al., 2020). Previous studies have found that the energy range of pulsating aurora electrons is substantially higher than other auroral types, ranging between 10s to 100s of keV (e.g., Whalen et al., 1971; Sandahl et al., 1980). Both the total energy flux and hardness can vary, even within individual events. Jones et al. (2009) notes often seeing a decrease in the differential energy flux of 0.5 to 32.5 keV electrons throughout an event. Hosokawa and Ogawa (2015) found, using the European Incoherent Scatter Radar, that the energy spectrum of pulsating aurora is harder when a patch is "on" versus when it is "off" with only background aurora present.

Some studies have attempted to classify different types of pulsating aurora. For instance, Royrvik and Davis (1977) classified events into patches, arcs, and arc segments. More recently, Grono and Donovan (2018) made a distinction between the quickly varying amorphous pulsating aurora (APA), more regular patchy pulsating (PPA) aurora, and non-pulsating patchy aurora (nPPA). Tesema et al. (2020) used incoherent scatter radar to look at the electron density profile between APA, PPA, and nPPA. They found that PPA and nPPA were associated with enhanced electron densities below 100 km when compared with APA.

Several papers regarding the the height of pulsating aurora indicate that there may be a relation between peak differential energy flux of precipitating electrons and substorm onset. In the two events that Oyama et al. (2017) analyzed, they found a drop to lower altitudes following substorm onset in the atmospheric electron densities of pulsating aurora. This would indicate an influx of higher energy electrons capable of penetrating further into the atmosphere. These results are similar to the statistical study of Hosokawa and Ogawa (2015) who showed that the electron density profile of pulsating aurora extends lower in altitude during periods with a large AE index (> 500). This previous work is a strong indicator of the increase in higher energy electrons, or hardening, during geomagnetic activity that causes an increase in AE index. However, the results are qualitative as altitude is only a proxy for energy. Wing et al. (2013) did conduct a statistical study of auroral energies associated with substorm onset. They made distinctions between broadband (Alfvén accelerated) electrons, monoenergetic (parallel electric field accelerated) electrons, and diffuse (whistler mode wave scattered) electrons. They found that total energy flux increases in association to substorm onset for all types, with the largest for diffuse electrons. However, they made no distinction between general diffuse and pulsating aurora.

These previous investigations make a strong case for a link between substorm onset and AE index and both the total energy flux and spectral hardness of pulsating aurora. More energetic events seem to occur right after substorm onset and for higher AE indices. However, direct evidence supporting this hypothesis has yet to be established. Providing this evidence will be an important step in understanding how energy is transferred from the magnetosphere to the atmosphere. There are many reasons why this is important, but one which has recently become more apparent is the depletion of ozone due to pulsating aurora produced NO_x (Turunen et al., 2016; Verronen et al., 2021). In this paper, we provide statistical evidence, using inverted differential energy fluxes, that substorm onset and AE index are indeed correlated with a higher differential energy flux and a harder energy content in pulsating aurora. The results shown here both confirm the high-energy nature of pulsating aurora and specify how pulsating aurora energies are correlated with substorm onset and AE index.

2 Data

This paper presents a data set of 57 pulsating aurora events between 2012 and 2021, four of which (2015-01-13, 2017-08-17, 2018-12-30, and 2021-01-13) were not usable for our energy inversion. We visually identified pulsating aurora using all sky images and used the classifications of both (Royrvik & Davis, 1977) and (Grono & Donovan, 2018) when doing so. This data was captured over 51 days with the Poker Flat Research Range All Sky Imager (PFRR ASI). A table with the dates of all 51 days can be found in the supplemental material and the data can be found in Troyer et al. (2022). This instrument takes an image approximately every 12 seconds at 428 nm, 557 nm, and 630 nm. We used the 428 nm images. It is worth noting that despite the 12 second period of the camera, we can still accurately identify pulsating aurora, see Figure 1 panels A1-A3 as an example.

For each of these pulsating aurora events, the Poker Flat Incoherent Scatter Radar (PFISR) was running one of the D-region modes (MSWinds23, MSWinds26, or MSWinds27). For more details about these modes than we describe here, see Kaeppler et al. (2020). These modes all use 13-baud Barker codes with 10 μs baud, oversampled at 5μs (0.75 km range resolution) to provide electron density as function of range and time over ranges between 40 to 144 km. This study uses one minute integration times, which means the electron density profiles are averaged over many cycles of the pulsating aurora. These modes all use four beam directions (magnetic zenith, vertical, north-west, and north-east). This study uses the vertical beam data since it is systematically more sensitive than the magnetic zenith direction at PFISR. The magnetic zenith is close to the phased-array antenna grating lobe steering limit. Furthermore, the MSWinds27 modes revisit the beams unevenly such that the vertical beam receives 16 times more pulses than the other beam directions, resulting in a factor of 4 improvement in the statistical uncertainty relative to the other beam directions. The vertical beam is $< 20^\circ$ away from the magnetic zenith direction which is sufficiently small for our inversions to neglect any variations across magnetic field lines. Supplementary Appendix 2 gives additional information on the PFISR experiments and data processing. Figure 1 panel B shows an example of electron densities measured by PFISR MSWinds23 during a period of typical pulsating aurora on October 13, 2016. This event began less than 15 minutes after a substorm onset and continued until the end of the PFISR experiment.

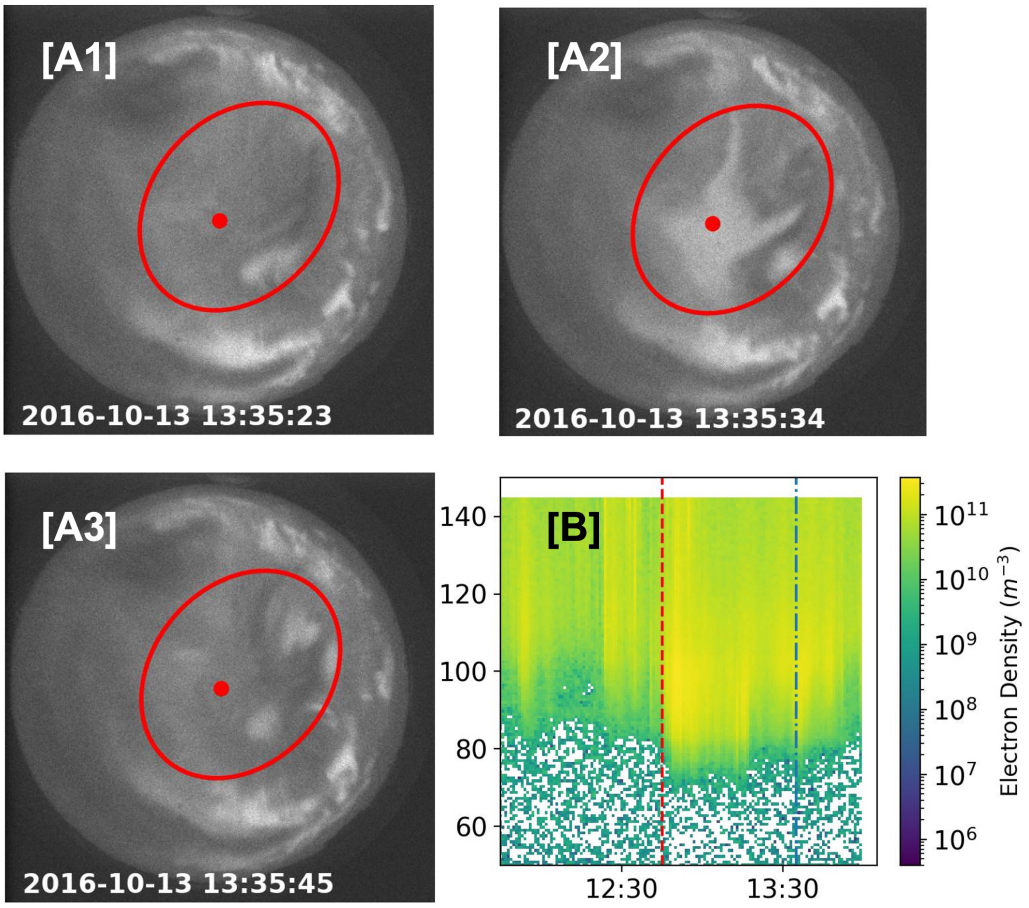

Figure 1. Panels A1-A3 show a series of 428 nm images from the Poker Flat Research Range All Sky Imager with several pulsating aurora patches of differing sizes. Even though the imaging rate is 12 seconds, we can still identify pulsating aurora. The red dot indicates the center of each image and thus the approximate location of the vertical PFISR beam. Panel B is the PFISR electron number density data for a pulsating aurora event on October 13, 2016. The data is plotted vs. altitude in km and universal time. The dashed red line indicates the start of pulsating aurora. The dashed and dotted blue line indicates when the images were taken. The radar stopped taking data before the pulsating aurora ended.

3 Analysis

In this study, we quantify the differential energy flux of pulsating aurora, in particular, the higher energy portion. Previous investigations have indicated that the energy of pulsating aurora varies significantly both within and between events, often associated with substorm activity (Jones et al., 2009; Wing et al., 2013; Hosokawa & Ogawa, 2015). Based on these results, we chose to examine variations related to magnetic local time (MLT), AE index, and an epoch associated with temporal substorm proximity. We set an epoch time of 0 to substorm onsets taken from lists created by Newell and Gjerloev (2011), Forsyth et al. (2015), and Ohtani and Gjerloev (2020). We chose these three lists because they cover a time period that covers the range of dates in our data. Each method identifies substorms in a slightly different way, so by including all three we can identify more events over a broader range of criteria. We limited these substorms to those that occurred within $\pm 15^\circ$ longitude and $\pm 8^\circ$ latitude of the Poker Flat Research Range. For the AE indices, we used archived 10-minute averaged predicted values (Luo et al., 2013). For every 1-minute electron density profile we find the closest in time AE index and assign that to the data point.

As a proxy for energy, we chose the lower altitude boundary that PFISR measured a number density of $N_e = 10^{10}\,\mathrm{m}^{-3}$ for each 1-minute integrated altitude profile. Additionally, to meet this criteria, the associated error had to be less than $5 \times 10^9\,\mathrm{m}^{-3}$. We chose these values somewhat arbitrarily given that they are round numbers near the detection limit of PFISR. However, we did test the sensitivity and found them to be acceptably insensitive. Future, more sensitive instruments could use a smaller density threshold and thus detect lower altitudes. Finally, we implemented an outlier-rejection algorithm to remove high power returns that are not consistent with the expected electron density profile from precipitation. The D-region data can be cluttered by range-aliased satellite echoes, airplanes in antenna sidelobes, and various types of interference. Most of these clutter sources appear as localized outliers in the power data confined to one or two range-gates. We expect a realistic electron density profile to extend over 10s of km in altitude and be monotonically decreasing with altitude. We compute the median electron density over 5 km around a data point and check that it is less than the median electron density 20 km above that point. Furthermore, we check if there are any NaN or negative electron density estimates in the 20 km above that point.

It is more typical for studies to concentrate on the altitude of the peak electron density. We chose a different metric as we wanted a proxy that would more closely represent the flux of higher energy particles. This approach isn't perfect as a higher flux of slightly lower energy particles could produce a similar boundary to a lower flux of higher energy particles. Any altitude metric is still only a proxy for energy, but this one also contains other useful information. One of the main goals of this work is to provide data to help understand the atmospheric effects of pulsating aurora such as ozone depletion. In this regard, atmospheric changes are more important than the original energy flux. Thus, by choosing to measure altitude from a lower boundary instead of the peak electron density, we are able to more closely connect our measurements to possible atmospheric effects.

3.1 Magnetic Local Time

Figure 2 panel A shows the altitude boundary values compared to MLT as calculated from the IGRF model for 2020. As we would expect, a majority of the measurements occurred several hours after magnetic midnight. Previous studies have shown that this is the most common time for pulsating aurora (Oguti et al., 1981; Jones et al., 2011). The hourly averages shown by the black diamonds centered on each hour indicate that there is little, if any, dependence on MLT. Interestingly, previous results have shown a small correlation between peak electron density altitude and MLT (Hosokawa & Ogawa, 2015; Partamies et al., 2017; E. C. Bland et al., 2019; Tesema et al., 2020; Nanjo et al., 2021). It's possible that our data is obscuring this trend due to the wide scatter of data and limited statistics for several time bins. In addition, we requested instrument runs during the most common time for pulsating aurora, so the data is biased towards that period.

3.2 Substorm Onset and AE index

Figure 2 panel B shows the altitude boundary with $N_e = 10^{10}\,\mathrm{m}^{-3}$ compared to substorm onset. Here we see that lower altitudes are more common closer to substorm onset, indicating a hardening of the energy content. These results are similar to that of Oyama et al. (2017), who found both an enhancement and lowering of electron densities just after substorm onsets for several case study pulsating aurora events. Our work extends these findings to a statistical dataset.

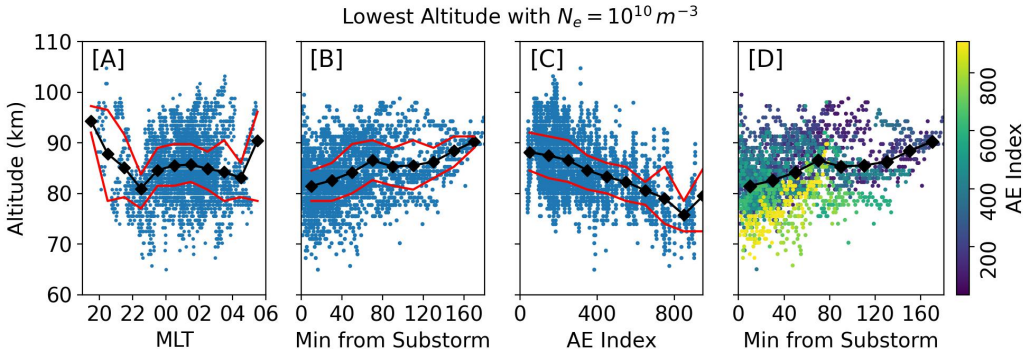

Figure 2. Lowest altitude PFISR measurements during pulsating aurora with $N_e = 10^{10}\,\mathrm{m}^{-3}$ plotted versus magnetic local time [A], time from the nearest substorm onset [B], AE index [C], and combined substorm and AE [D]. The black diamonds indicate the average altitude for the surrounding hour, 20 minutes, 200 AE units, and 20 minutes respectively. The red lines indicate the 25% and 75% quartiles.

Figure 2 panel C shows the altitude boundary with $N_e = 10^{10}\,\mathrm{m}^{-3}$ compared to the closest in time 10-minute averaged AE index. Similar to substorm proximity, there is a clear relation between a higher AE value and lower altitudes. This is similar to the results of Hosokawa and Ogawa (2015) who found that the peak altitude of pulsating aurora lowers during higher AE indices. However, our measurements differ in that the peak altitude is a proxy for an average energy flux, whereas our lower altitude boundary is more representative of the energy content hardness.

We combined Figures 2B and 2C to produce Figure 2 panel D. Here we have colored the markers of Figure 2B based on AE index. This result shows that both temporal substorm proximity and AE index play a role in varying the lower altitude boundary. The lowest altitudes tend to occur with both a high AE index and close temporal proximity to a substorm. In regards to the statistics, our events cover a wide range of AE indices with 10 occurring during periods with AE > 600 and of those 3 with AE $>$ 800.

We also performed a similar analysis using AL indices, but the results did not differ in any meaningful way. A more negative AL index corresponded to lower altitudes. This plot can be found in the supplementary materials.

3.3 Energy Spectra from Electron Density Inversion

Our analysis of the lower altitude boundary with $N_e = 10^{10}\,\mathrm{m}^{-3}$ indicates that both AE index and substorm onset have significant impacts on how hard the pulsating aurora energy content can be. However, this metric is only a proxy for hardness. To investigate further, we solved the inverted problem required to convert the PFISR electron densities into a differential energy flux. To do this, we used the process outlined in Semeter and Kamalabadi (2005). In doing so, we assumed that the pitch angle distribution was isotropic (Whalen et al., 1971; Sandahl et al., 1980), and that the electron density varies slowly compared to the 1-minute PFISR integration time scales. We describe our exact implementation of the inversion process in supplementary Appendix 1. In an analysis like this, there are multiple spectra that could result in a reasonably good fit of the density profile, making the problem ill-defined. To help mitigate this, we chose the solution that maximized the Berg Entropy. As Semeter and Kamalabadi (2005) states, this solution "may be viewed as the most noncommittal approach with respect to the unavailable information." Because of these uncertainties that are inherent to the inversion process, it is not useful to look at the finer shape of the differential energy flux. Instead, to provide a more robust analysis, we chose an energy threshold of 30 keV to separate the low and high portions of the differential energy flux and integrated the two regions. This gives us an average low and high energy flux and limits the dependency of our results on the smaller scale details.

The largest source of error in the inversion process is likely the assumed atmospheric chemistry that connects PFISR observations to an ionization rate. This is still an ongoing area of research, especially for the D-region. As our primary chemistry model we used the Glukhov-Pasko-Inan (GPI) model (Glukhov et al., 1992; Lehtinen & Inan, 2007). This has been shown to perform well for the D-region (Marshall et al., 2019). For the E-region, we set the values above 90 km to those calculated by Gledhill (1986) for nighttime aurora. The Gledhill model is suitably close that of Vickrey et al. (1982) above 90 km and the Vickrey model has been shown to perform well in this region (Sivadas et al., 2017). While we could have used the Vickrey model, we believe the Gledhill model is more relevant for this data. However, both models are only rough estimates. We refer to this adjusted model as GPI+. To provide context to our results calculated using GPI+, we inverted each density profile using three additional chemistry models. These results, along with other possible sources of errors, can be found in the supplementary Appendix.

After performing the inversions, we found the geometric mean for ≥ 30 keV and < 30 keV electrons in bins relative to substorm onset and AE index. Figure 3 shows the results and demonstrates the link between energy and substorm activity. This figure shows how the energy composition of pulsating aurora varies with respect to both substorm proximity [A] and AE index [B]. Within an hour of a substorm around a third of the total differential energy flux is carried by ≥ 30 keV electrons. At > 60 minutes this drops to around a sixth. Interestingly, while the total differential energy flux climbs closer to the substorm, the energy composition remains similar all the way out to an hour after onset. This indicates that the initial substorm "kick" hardens the energy content and it remains hard up to an hour afterwards, even as the total differential energy flux decreases.

The differential energy flux associated with AE index varies even more dramatically. In highly perturbed times of AE > 600 over a half of the average differential energy flux is carried by the ≥ 30 keV electrons. This again drops to just over a tenth for quiet periods of AE ≤ 200. We also looked at the differential energy flux relative to AL indices, but found no difference to AE beyond a few percent.

Assumptions about the atmospheric chemistry can vary the absolute differential energy flux, but for every model we found the same relative behavior. While not shown here, the relative behavior was also the same when we used threshold values of 50 keV and 100 keV. For < 20 min the high energy contributions were 13.9% and 1.2% respectively. For > 600 AE these were 37.8% and 2.4% respectively. Thus, we speculate with a high level of confidence that pulsating auroral energy content is varied by both the strength of a substorm as well as temporal proximity to it.

4 Discussion

Our work builds on the likes of Wing et al. (2013), Hosokawa and Ogawa (2015), and Oyama et al. (2017), whose studies showed that the altitude of pulsating aurora can lower after substorm onset and for periods of high AE index. It also builds on papers such as Jones et al. (2009), which demonstrated that the inverted differential energy flux of particular pulsating aurora events can vary throughout the event duration. This past work provides evidence that the total energy flux and spectral hardness of pulsating au-

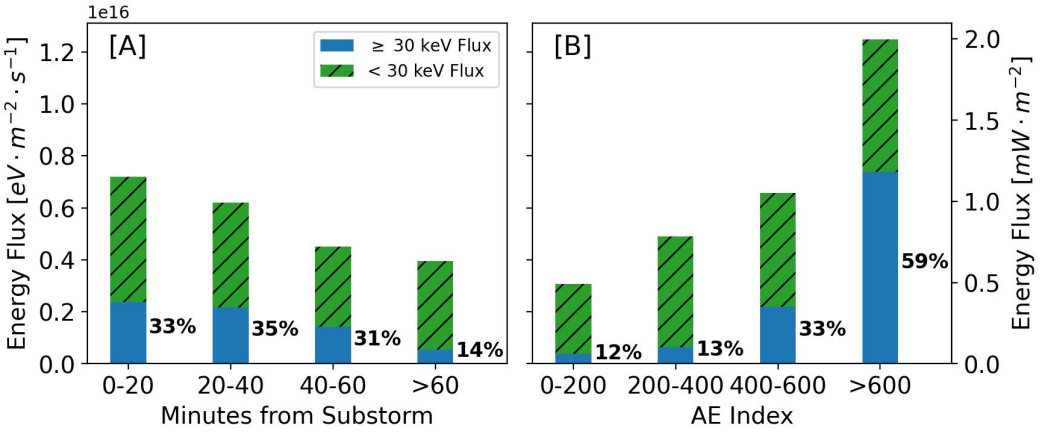

Figure 3. The high ($\geq$ 30 keV) and low ($<$ 30 keV) differential energy flux contributions to pulsating aurora events occurring in four temporal bins relative to substorm onset [A] and AE index [B].

rora could be influenced by substorm onset and AE index, but does not make a direct statistical connection.

The results shown in Figure 3 are significant as they provide a statistical connection in several ways. First, they show that the total differential energy flux of pulsating aurora is highly variable. Second, they show that pulsating aurora events can have large, and in some cases majority, contributions from $\geq$ 30 keV electrons, which represents a hard energy content relative to other auroral types. Third, they show that these quantities are strongly correlated with substorm onset and AE index. These statistical links have never been demonstrated before with inverted differential energy flux and they suggest a process connecting substorms and pulsating aurora.

The link between substorms and pulsating aurora is likely through whistler-mode waves, which are known to drive instances of pulsating aurora (Nishimura et al., 2010, 2011; Jaynes et al., 2013; Kasahara et al., 2018; Hosokawa et al., 2020). There is a well documented relation between substorm activity post-midnight and whistler-mode wave generation near the equator (Tsurutani & Smith, 1974; Thorne et al., 1974). The proposed mechanism connecting them is Doppler-shifted cyclotron resonance with 10-100 keV substorm injected electrons (Dungey, 1963; Kennel & Petschek, 1966). In addition, the amplitude of already present whistler-mode waves can vary with substorm injection. Meredith et al. (2000) showed that between 3.8 $< L <$ 6 whistler-mode amplitudes

increased after a substorm and then decayed with a timescale of $\tau \approx 1.1$ hours. It is highly speculative, but that value is similar to the timescale over which we see a decrease in the ≥ 30 keV contributions. Given that whistler-mode waves are known to drive pulsating aurora, could this be one likely explanation? Additional work will be needed to ascertain how relevant this connection is.

The results in Figure 3 are also important in that they confirm the inherent energetic nature of pulsating aurora that previous case studies have suggested. One important reason to study pulsating aurora are the impacts they can have on our atmosphere. Pulsating aurora are very common (Oguti et al., 1981) and can be long-lasting (Jones et al., 2013), thus they could represent an important transfer of energy between the magnetosphere and lower ionosphere. When considering the effects of this transfer, the total energy flux is clearly important, but so too is the contributions from electrons with energies ≥ 30 keV. Higher energy electrons reach further into the atmosphere and thus have a higher probability of influencing terrestrial climate through processes like NO_x based ozone depletion (Turunen et al., 2016; Verronen et al., 2021, & and references therein). We found that the hardest events occur close in time to substorm onset and for high AE indices. In short, our results can be used to more accurately parameterize the atmospheric consequences of pulsating aurora. For instance, combining the results of Figure 3 with those of E. Bland et al. (2021), we can perform a back-of-the-envelope calculation to estimate the incoming power of a typical pulsating aurora event. We will assume an event extending between 62° and 70° magnetic latitude and 4 hours of magnetic local time. Using this, approximately 4.8 gigawatts (GW) of power would be entering the atmosphere during periods with AE > 600 with 2.8 GW coming from ≥ 30 keV electrons. For periods < 20 minutes after substorm onset and all AE indices these values are 2.5 GW and 0.8 GW respectively.

A savvy reader might notice that in Figure 2B it appears that within 20 minutes of substorm onset, what could be considered the expansion phase, is the most common time for our pulsating aurora. That statistic seems to be in contradiction to Partamies et al. (2017), who found that the most common substorm phase for pulsating aurora was the recovery phase. While occurrence rates was not the focus of this work, it is worth examining where this difference could come from. There are two potential reasons. One, our search for pulsating aurora differs. Partamies et al. (2017) only identified pulsating aurora when it was the most dominant type, stating that "...our event selection crite-

ria favors recovery phases over the expansion phases where brighter aurora plays a major role in the auroral displays." Our search included pulsating aurora if we could identify it directly overhead, even when it was not the most visually dominant aurora. Two, Partamies et al. (2017) used a magnetometer at the imager locations while our search was semi local and encompassed a much larger geographic region, so we likely included more substorms in our data set.

Finally, we wanted to point out that other metrics can vary the energy of pulsating aurora besides the ones we looked at. Perhaps most interestingly is the type of pulsating aurora. As Tesema et al. (2020) found, the electron density profile, and thus likely the energy, varies between the types identified by Grono and Donovan (2018). Given the image frequency of our data, we could not accurately distinguish between the different types. However, future studies including pulsating aurora type along with substorm onset and AE index might see an even stronger correlation.

5 Summary

In the field of pulsating aurora, it has been suspected that substorm onset and AE index are linked to variations in the energy flux of the incoming electrons. These suspicions have arisen from studies investigating proxies for energy, such as the altitude of the peak electron density. In this paper, we presented statistical evidence, using inverted energy content, that this hypothesis is correct. When pulsating aurora occurs soon after a substorm onset it is more likely to have a larger total differential energy flux and a harder energy content. This same behaviour also occurs for higher AE indices.

- The differential energy flux of pulsating aurora correlates strongly with the substorm onset and AE index.
- In relation to substorm onset the total differential energy flux varies between 1.15 and 0.63 $\mathrm{mW \cdot m^{-2}}$ for $\leq$ 20 and $>$ 60 minutes. The associated contribution to the total differential energy flux from $\geq$ 30 keV electrons are 33% and 14%.
- In relation to substorms, the differential energy flux remains hard out to 1 hour after onset before softening.
- In relation to AE index the total differential energy flux varies between 2.00 and 0.49 $\mathrm{mW \cdot m^{-2}}$ for $>$ 600 and $\leq$ 200 AE indices. The associated contributions to the total differential energy flux from $\geq$ 30 keV electrons are 59% and 12%.

- We estimate that for a typically pulsating auroral event occurring < 20 min after substorm onset (AE > 600), approximately 2.5 (4.8) GW of power enters the atmosphere. The contributions from ≥ 30 keV electrons are 0.8 (2.8) GW.

Acknowledgments

We acknowledge the help and advice of Robert Marshall, Nithin Sivadas, and Pekka Verronen in developing our inversion analysis.

We acknowledge the substorm timing list identified by the SOPHIE technique (Forsyth et al., 2015), the Newell and Gjerloev technique (Newell & Gjerloev, 2011), the Ohtani and Gjerloev technique (Ohtani & Gjerloev, 2020), the SMU and SML indices (Newell & Gjerloev, 2011); and the SuperMAG collaboration (Gjerloev, 2012).

This material is based upon work supported by the Poker Flat Incoherent Scatter Radar, which is a major facility funded by the National Science Foundation through cooperative agreement AGS-1840962 to SRI International.

RNT was supported by the NASA FINESST award 80NSSC20K1514 to the University of Iowa.

ANJ was supported by NSF CAREER grant 2045016 to the University of Iowa.

SRK was supported by Air Force Office of Scientific Research grant FA9550-19-1-0130 to Clemson University.

Open Research

Imager data referenced in this paper is available from `https://doi.org/10.5281/zenodo.6878145` and was derived from the University of Alaska Fairbanks Geophysical Institute archive.

The incoherent scatter radar data referenced in this paper is available from AMISR: `https://data.amisr.com/database/pfisr/level2/nenotr/0.9.2018.11.22/`

The AE and AL indices referenced in this paper are available from LASP: `https://lasp.colorado.edu/space_weather/dsttemerin/archive/dst_years.html`

The substorm onset lists referenced in this paper are available from SuperMAG: `https://supermag.jhuapl.edu/substorms/?tab=download`

References

Bland, E., Tesema, F., & Partamies, N. (2021, February). D-region impact area of energetic electron precipitation during pulsating aurora. *Annales Geophysicae*, *39*(1), 135-149. doi: 10.5194/angeo-39-135-2021

Bland, E. C., Partamies, N., Heino, E., Yukimatu, A. S., & Miyaoka, H. (2019, July). Energetic Electron Precipitation Occurrence Rates Determined Using the Syowa East SuperDARN Radar. *Journal of Geophysical Research (Space Physics)*, *124*(7), 6253-6265. doi: 10.1029/2018JA026437

Davis, T. N. (1978, January). Observed microstructure of auroral forms. *Journal of Geomagnetism and Geoelectricity*, *30*(4), 371-380. doi: 10.5636/jgg.30.371

Dungey, J. W. (1963, June). Loss of Van Allen electrons due to whistlers. *Planetary and Space Science*, *11*(6), 591-595. doi: 10.1016/0032-0633(63)90166-1

Forsyth, C., Rae, I. J., Coxon, J. C., Freeman, M. P., Jackman, C. M., Gjerloev, J., & Fazakerley, A. N. (2015, December). A new technique for determining Substorm Onsets and Phases from Indices of the Electrojet (SOPHIE). *Journal of Geophysical Research (Space Physics)*, *120*(12), 10,592-10,606. doi: 10.1002/2015JA021343

Gjerloev, J. W. (2012, September). The SuperMAG data processing technique. *Journal of Geophysical Research (Space Physics)*, *117*(A9), A09213. doi: 10.1029/2012JA017683

Gledhill, J. A. (1986, June). The effective recombination coefficient of electrons in the ionosphere between 50 and 150 km. *Radio Science*, *21*(3), 399-408. doi: 10.1029/RS021i003p00399

Glukhov, V. S., Pasko, V. P., & Inan, U. S. (1992, November). Relaxation of transient lower ionospheric disturbances caused by lightning-whistler-induced electron precipitation bursts. *Journal of Geophysical Research*, *97*(A11), 16971-16979. doi: 10.1029/92JA01596

Grono, E., & Donovan, E. (2018, June). Differentiating diffuse auroras based on phenomenology. *Annales Geophysicae*, *36*(3), 891-898. doi: 10.5194/angeo-36-891-2018

Hosokawa, K., Miyoshi, Y., Ozaki, M., Oyama, S. I., Ogawa, Y., Kurita, S., ... Fujii, R. (2020, February). Multiple time-scale beats in aurora: precise orchestration via magnetospheric chorus waves. *Scientific Reports*, *10*, 3380. doi:

10.1038/s41598-020-59642-8

Hosokawa, K., & Ogawa, Y. (2015, July). Ionospheric variation during pulsating aurora. *Journal of Geophysical Research (Space Physics)*, *120*(7), 5943-5957. doi: 10.1002/2015JA021401

Jaynes, A. N., Lessard, M. R., Rodriguez, J. V., Donovan, E., Loto'Aniu, T. M., & Rychert, K. (2013, August). Pulsating auroral electron flux modulations in the equatorial magnetosphere. *Journal of Geophysical Research (Space Physics)*, *118*(8), 4884-4894. doi: 10.1002/jgra.50434

Johnstone, A. D. (1978, July). Pulsating aurora. *Nature*, *274*(5667), 119-126. doi: 10.1038/274119a0

Jones, S. L., Lessard, M. R., Fernandes, P. A., Lummerzheim, D., Semeter, J. L., Heinselman, C. J., ... Asamura, K. (2009, May). PFISR and ROPA observations of pulsating aurora. *Journal of Atmospheric and Solar-Terrestrial Physics*, *71*(6-7), 708-716. doi: 10.1016/j.jastp.2008.10.004

Jones, S. L., Lessard, M. R., Rychert, K., Spanswick, E., & Donovan, E. (2011, March). Large-scale aspects and temporal evolution of pulsating aurora. *Journal of Geophysical Research (Space Physics)*, *116*(A3), A03214. doi: 10.1029/2010JA015840

Jones, S. L., Lessard, M. R., Rychert, K., Spanswick, E., Donovan, E., & Jaynes, A. N. (2013, June). Persistent, widespread pulsating aurora: A case study. *Journal of Geophysical Research (Space Physics)*, *118*(6), 2998-3006. doi: 10.1002/jgra.50301

Kaeppler, S. R., Sanchez, E., Varney, R. H., Irvin, R. J., Marshall, R. A., Bortnik, J., ... Reyes, P. M. (2020). Chapter 6 - incoherent scatter radar observations of 10–100kev precipitation: review and outlook. In A. N. Jaynes & M. E. Usanova (Eds.), *The dynamic loss of earth's radiation belts* (p. 145-197). Elsevier. Retrieved from `https://www.sciencedirect.com/science/article/pii/B9780128133712000068` doi: https://doi.org/10.1016/B978-0-12-813371-2.00006-8

Kasahara, S., Miyoshi, Y., Yokota, S., Mitani, T., Kasahara, Y., Matsuda, S., ... Shinohara, I. (2018, February). Pulsating aurora from electron scattering by chorus waves. *Nature*, *554*(7692), 337-340. doi: 10.1038/nature25505

Kennel, C. F., & Petschek, H. E. (1966, January). Limit on Stably Trapped Particle

Fluxes. *Journal of Geophysical Research (Space Physics)*, *71*, 1. doi: 10.1029/JZ071i001p00001

Lehtinen, N. G., & Inan, U. S. (2007, April). Possible persistent ionization caused by giant blue jets. *Geophysical Review Letters*, *34*(8), L08804. doi: 10.1029/2006GL029051

Lessard, M. R. (2012). A review of pulsating aurora. In *Auroral phenomenology and magnetospheric processes earth and other planets* (Vol. 197, pp. 5673–68). Washington, D.C. :: American Geophysical Union.

Luo, B., Li, X., Temerin, M., & Liu, S. (2013, December). Prediction of the AU, AL, and AE indices using solar wind parameters. *Journal of Geophysical Research (Space Physics)*, *118*(12), 7683-7694. doi: 10.1002/2013JA019188

Marshall, R. A., Xu, W., Kero, A., Kabirzadeh, R., & Sanchez, E. (2019, February). Atmospheric effects of a relativistic electron beam injected from above: chemistry, electrodynamics, and radio scattering. *Frontiers in Astronomy and Space Sciences*, *6*, 6. doi: 10.3389/fspas.2019.00006

Meredith, N. P., Horne, R. B., Johnstone, A. D., & Anderson, R. R. (2000, June). The temporal evolution of electron distributions and associated wave activity following substorm injections in the inner magnetosphere. *Journal of Geophysical Research*, *105*(A6), 12907-12918. doi: 10.1029/2000JA900010

Nanjo, S., Hozumi, Y., Hosokawa, K., Kataoka, R., Miyoshi, Y., Oyama, S.-i., ... Kurita, S. (2021, October). Periodicities and Colors of Pulsating Auroras: DSLR Camera Observations From the International Space Station. *Journal of Geophysical Research (Space Physics)*, *126*(10), e29564. doi: 10.1029/2021JA029564

Newell, P. T., & Gjerloev, J. W. (2011, December). Substorm and magnetosphere characteristic scales inferred from the SuperMAG auroral electrojet indices. *Journal of Geophysical Research (Space Physics)*, *116*(A12), A12232. doi: 10.1029/2011JA016936

Nishimura, Y., Bortnik, J., Li, W., Thorne, R. M., Chen, L., Lyons, L. R., ... Auster, U. (2011, November). Multievent study of the correlation between pulsating aurora and whistler mode chorus emissions. *Journal of Geophysical Research (Space Physics)*, *116*(A11), A11221. doi: 10.1029/2011JA016876

Nishimura, Y., Bortnik, J., Li, W., Thorne, R. M., Lyons, L. R., Angelopoulos, V.,

494 ... Auster, U. (2010, October). Identifying the Driver of Pulsating Aurora.
495 *Science*, *330*(6000), 81. doi: 10.1126/science.1193186

496 Oguti, T., Kokubun, S., Hayashi, K., Tsuruda, K., Machida, S., Kitamura, T., ...
497 Watanabe, T. (1981, August). Statistics of pulsating auroras on the basis of
498 all-sky TV data from five stations. I. Occurrence frequency. *Canadian Journal*
499 *of Physics*, *59*, 1150-1157. doi: 10.1139/p81-152

500 Ohtani, S., & Gjerloev, J. W. (2020, September). Is the Substorm Current
501 Wedge an Ensemble of Wedgelets?: Revisit to Midlatitude Positive Bays.
502 *Journal of Geophysical Research (Space Physics)*, *125*(9), e27902. doi:
503 10.1029/2020JA027902

504 Oyama, S., Kero, A., Rodger, C. J., Clilverd, M. A., Miyoshi, Y., Partamies, N., ...
505 Saito, S. (2017, June). Energetic electron precipitation and auroral morphol-
506 ogy at the substorm recovery phase. *Journal of Geophysical Research (Space*
507 *Physics)*, *122*(6), 6508-6527. doi: 10.1002/2016JA023484

508 Partamies, N., Whiter, D., Kadokura, A., Kauristie, K., Nesse Tyssøy, H., Massetti,
509 S., ... Raita, T. (2017, May). Occurrence and average behavior of pulsating
510 aurora. *Journal of Geophysical Research (Space Physics)*, *122*(5), 5606-5618.
511 doi: 10.1002/2017JA024039

512 Royrvik, O., & Davis, T. N. (1977, October). Pulsating aurora: Local and global
513 morphology. *Journal of Geophysical Research*, *82*(29), 4720. doi: 10.1029/
514 JA082i029p04720

515 Sandahl, I., Eliasson, L., & Lundin, R. (1980, May). Rocket observations of precip-
516 itating electrons over a pulsating aurora. *Geophysical Research Letters*, *7*(5),
517 309-312. doi: 10.1029/GL007i005p00309

518 Semeter, J., & Kamalabadi, F. (2005, April). Determination of primary electron
519 spectra from incoherent scatter radar measurements of the auroral E region.
520 *Radio Science*, *40*(2), RS2006. doi: 10.1029/2004RS003042

521 Sivadas, N., Semeter, J., Nishimura, Y., & Kero, A. (2017, October). Simultaneous
522 Measurements of Substorm-Related Electron Energization in the Ionosphere
523 and the Plasma Sheet. *Journal of Geophysical Research (Space Physics)*,
524 *122*(10), 10,528-10,547. doi: 10.1002/2017JA023995

525 Tesema, F., Partamies, N., Nesse Tyssøy, H., & McKay, D. (2020, November). Ob-
526 servations of precipitation energies during different types of pulsating aurora.

Annales Geophysicae, *38*(6), 1191-1202. doi: 10.5194/angeo-38-1191-2020

Thorne, R. M., Smith, E. J., Fiske, K. J., & Church, S. R. (1974, January). Intensity variation of ELF hiss and chorus during isolated substorms. *Geophysical Research Letters*, *1*(5), 193-196. doi: 10.1029/GL001i005p00193

Troyer, R., Jaynes, A., Kaeppler, S., Varney, R., Reimer, A., & Jones, S. (2022). *PFRR ASC Image Dataset for Troyer et al. 2022 (Substorm Activity as a Driver of Energetic Pulsating Aurora).* `https://doi.org/10.5281/zenodo.6878145`. doi: 10.5281/zenodo.6878145

Tsurutani, B. T., & Smith, E. J. (1974, January). Postmidnight chorus: A substorm phenomenon. *Journal of Geophysical Research (Space Physics)*, *79*(1), 118-127. doi: 10.1029/JA079i001p00118

Turunen, E., Kero, A., Verronen, P. T., Miyoshi, Y., Oyama, S.-I., & Saito, S. (2016, October). Mesospheric ozone destruction by high-energy electron precipitation associated with pulsating aurora. *Journal of Geophysical Research (Atmospheres)*, *121*(19), 11,852-11,861. doi: 10.1002/2016JD025015

Verronen, P. T., Kero, A., Partamies, N., Szelag, M. E., Oyama, S.-I., Miyoshi, Y., & Turunen, E. (2021, October). Simulated seasonal impact on middle atmospheric ozone from high-energy electron precipitation related to pulsating aurorae. *Annales Geophysicae*, *39*(5), 883-897. doi: 10.5194/angeo-39-883-2021

Vickrey, J. F., Vondrak, R. R., & Matthews, S. J. (1982, July). Energy deposition by precipitating particles and Joule dissipation in the auroral ionosphere. *Journal of Geophysical Research*, *87*(A7), 5184-5196. doi: 10.1029/JA087iA07p05184

Whalen, B. A., Miller, J. R., & McDiarmid, I. B. (1971, January). Energetic particle measurements in a pulsating aurora. *Journal of Geophysical Research*, *76*(4), 978. doi: 10.1029/JA076i004p00978

Wing, S., Gkioulidou, M., Johnson, J. R., Newell, P. T., & Wang, C.-P. (2013, March). Auroral particle precipitation characterized by the substorm cycle. *Journal of Geophysical Research (Space Physics)*, *118*(3), 1022-1039. doi: 10.1002/jgra.50160

Date	Start Time (UTC)	End Time (UTC)
2012-03-28	10:25:28	12:46:49
2012-12-20	11:12:07	16:18:47
2013-03-24	10:52:26	12:38:36
2014-11-02	12:40:31	13:31:41
2015-01-13	11:26:42	11:59:50
2015-01-14	10:32:55	10:54:12
2015-01-26	7:49:39	8:18:41
2015-02-26	9:46:46	10:45:44
2015-02-26	12:29:40	14:03:29
2015-03-12	10:01:48	10:44:22
2016-10-10	11:11:54	11:59:55
2016-10-13	12:49:20	13:59:51
2016-10-16	11:47:46	12:59:54
2016-10-19	10:33:39	12:15:24
2016-11-02	12:10:36	12:59:52
2016-11-13	9:24:40	10:59:49
2016-11-25	10:00:02	10:59:52
2016-12-11	9:51:00	9:59:56
2016-12-20	8:59:47	10:59:56
2016-12-26	10:32:15	10:59:51
2017-01-06	8:32:02	8:59:51
2017-03-30	12:10:59	13:04:47
2017-04-14	12:00:04	12:58:46
2017-04-18	12:00:01	12:31:27
2017-08-17	8:08:43	8:43:34
2017-09-03	9:36:22	10:45:19
2017-09-03	11:10:50	13:00:10
2017-09-14	11:30:31	14:00:05
2017-09-18	8:34:19	8:59:50
2018-10-23	11:05:32	11:35:47
2018-12-30	11:10:22	11:53:21
2019-01-06	12:00:07	12:59:53
2019-01-07	12:00:00	12:59:54
2019-01-26	13:47:03	13:59:48
2019-01-31	13:00:10	13:59:54
2019-02-01	13:00:09	13:59:49
2019-02-28	13:50:41	16:01:17
2019-03-01	10:04:47	12:04:41
2019-03-02	6:44:08	7:20:41
2019-03-28	13:45:12	14:06:12
2019-03-31	13:00:02	13:39:53
2019-04-03	13:00:11	13:48:53
2019-09-01	7:36:54	8:09:04
2019-09-01	9:14:12	10:21:35

2019-09-01	11:39:50	13:15:49
2019-09-02	10:12:14	11:06:53
2019-09-03	12:28:43	13:19:55
2019-12-18	11:42:17	11:59:59
2019-12-19	8:23:32	9:46:10
2019-12-19	10:47:53	11:59:52
2020-01-04	11:36:36	12:47:11
2020-01-05	12:23:32	15:02:37
2020-01-31	11:51:52	13:22:28
2020-03-31	11:36:47	12:51:36
2020-03-31	13:00:22	13:54:27
2020-10-01	12:34:59	14:43:50
2021-01-13	11:08:54	14:26:32

Supporting Information for Substorm Activity as a Driver of Energetic Pulsating Aurora

R. N. Troyer [1], A. N. Jaynes [1], S. L. Jones [2], S. R. Kaeppler [3],

R. H. Varney [4], A. S. Reimer [5]

[1]Department of Physics and Astronomy, University of Iowa

[2]Formerly of NASA Goddard Space Flight Center

[3]Clemson University

[4]Department of Atmospheric and Oceanic Sciences, University of California, Los Angeles

[5]Formerly of SRI International

Contents of this file

1. Text S1
2. Table S1
3. Figure S3

Introduction There are two supplementary materials for the paper Substorm Activity as a Driver of Energetic Pulsating Aurora contained here. They are not necessary to the results or interpretation of results, but provide further context to the specifics of our analysis methods. The first includes two appendices. One for the inversion analysis we

used to extract a differential energy flux from electron density, and one for the specific nuances of the Poker Flat Incoherent Scatter Radar data. The second is a table of the dates and times of the conjunctions between pulsating aurora and the Poker Flat Incoherent Scatter Radar that we used. The third is a figure that replaces AE index with AL index for Figure 2 panel C in the main paper.

Text S1.

Appendix A Inversion Technique

To solve the inverted problem of extracting a differential energy flux from electron densities, we used the process outlined in Semeter and Kamalabadi (2005). We assumed the pitch angle distribution of the incoming electrons was isotropic and used the universal energy dissipation function (Λ) given in the paper. We took our range-energy function from Barrett and Hays (1976) as

$$R = 4.7 \times 10^{-6} + 5.36 \times 10^{-5} K^{1.67} - 0.38 \times 10^{-7} K^{-0.7} \qquad [\mathrm{kg \cdot m^{-2}}]$$

where K is the electron energy in keV. Using these, we can construct a matrix A, where

$$A_{ij} = \frac{\Lambda\left(\frac{s(z_i)}{R(K_j)}\right) \rho(z_i) K_j \Delta K_j}{35.5 R(K_j)}$$

where $s(z_i) = \sec(\theta) \int_{z_0}^{\infty} \rho(z)\, dz$ is the mass distance traveled by an electron as a function of altitude. We assumed the dip angle of the magnetic field, $\theta \approx 0$. We calculated the neutral atmospheric density $\rho(z)$ using the NRLMSISE00 model and approximated $z \to \infty$ as $z = 1000$ km (Hedin, 1991).

The matrix A relates the ion production rate (q) and the differential number flux (ϕ) via

$$q_i = A_{ij} \frac{\phi_j}{\Delta K_j}$$

As Fang et al. (2010) showed, using a range-energy function gives poor estimates of the ion production rate from electrons below 1 keV. However, the altitude range of the PFISR data means that there is very little, if any, contribution from these energies. Therefore, we assume that the range-energy function is a good enough estimate in this case.

Given that the inversion is done in terms of the ion production rate, we must convert our electron density into an ion production rate. Once we have done this we can compare the model to reality and perform the iterative process involved in the inversion. Important atmospheric chemistry is encapsulated in the conversion of electron density measured by PFISR to an ion production rate. This is especially relevant below 85 km, where the chemistry of ion production becomes increasingly complex (Mitra, 1981). There are several ways of handling the chemistry. For our primary results we used the Glukhov-Pasko-Ina (GPI) model (Glukhov et al., 1992; Lehtinen & Inan, 2007). This uses the specific conditions as measured by PFISR, and modeled by the International Reference Ionosphere (IRI-2016) and NRLMSISE-00. From this, it outputs an ion production rate as a function of altitude. This is what the algorithm compares to the modeled ion production rate.

Previous work has shown that GPI performs well for the D-region (Marshall et al., 2019). We set the values above 90 km to those of Gledhill (1986) for nighttime aurora. The Gledhill model is suitably close that of Vickrey, Vondrak, and Matthews (1982) above

90 km and the Vickrey model performs well in this region (Sivadas et al., 2017). While we could have used the Vickrey model, we believe the Gledhill model is slightly more accurate to this data. We refer to this adjusted model as GPI+. Given that the the chemistry in this region of the atmosphere is not well known, we also performed our analysis with three additional models to provide context.

1. The best fit from Vickrey et al. (1982) of multiple observations from several authors of α in the E-region.

$$\alpha(h) = 2.5 \times 10^{-12} e^{-h_{\mathrm{km}}/51.2} \qquad [\mathrm{m}^3 \cdot \mathrm{s}^{-1}]$$

To use this model we needed to extend it into the D-region, where it is not well defined.

2. The observations of Osepian, Kirkwood, Dalin, and Tereschenko (2009) during a solar proton event on January 17, 2005 at 9:50 UT. While these observations cover the D-region, they must be extended into the E-region. They also only cover a single event and that event is not pulsating aurora.

3. The best fit of Gledhill (1986) for nighttime aurora covering the E-region and D-region.

$$\alpha(h) = 4.3 \times 10^{-6} e^{-2.42 \times 10^{-2} h_{\mathrm{km}}} + 8.16 \times 10^{12} e^{-0.524 h_{\mathrm{km}}} \qquad [\mathrm{cm}^3 \cdot \mathrm{s}^{-1}]$$

Figure S1 shows how these three additional chemistry model compare with our analysis. They are represented by scatter points around each bar. These points can be considered as rough bounds on our results.

To determine the differential number flux (ϕ) we iterated using the maximum entropy method outlined in Semeter and Kamalabadi (2005). We monitored convergence through the χ^2 value between the modeled ion production rate and the rate calculated from the

PFISR measurements. We stopped iterating when the step difference in the χ^2 values was less than 0.01. This usually took between 100 and 1000 steps. From the spectra that converged, we took those with a $1 \leq \chi^2_{\text{reduced}} < 3$ to be suitably good models. To calculate χ^2 it is important to have an accurate description of the variances (errors) in the PFISR data. The data products contain absolute errors associated with the measured number density. To propagate this to the ion production rate we calculated an intermediary recombination coefficient using the simple continuity equation

$$\frac{dn}{dt} = q - \alpha n^2$$

Assuming the temporal change of the electron density, as measured by PFISR, is small compared to the timescales we are studying, we can say that $q = \alpha n^2$, where α is the effective recombination coefficient. From our experience, this steady state assumption is good for pulsating aurora, at least when integrated over 1 minute like the PFISR data is. Previous work has also used it to convert between D-region electron densities and ion production rates (Kirkwood & Osepian, 1995; Osepian et al., 2009). Using this, our errors were then

$$\Delta q_{\text{chem}}(z) = 2\alpha(z)n(z)\Delta n(z)$$

To determine χ^2_{reduced} we need an estimate of the degrees of freedom in the model. We set this as the number of altitude bins where the errors were less than the data (fitted values) minus the number of energy bins (varied values). Figure S2 shows an example fitted electron density using this method. For this visualization, we converted back to electron density from the ion production rates using the same steady state assumption as above.

When performing the inversion, we found that the differential number flux of the highest energy bin was often over an order of magnitude larger than the next highest bin. We believe this is not physical and instead an artifact due to the initial electron density guess only needing to converge to the PFISR sensitivity ($\sim 10^9\,\mathrm{m}^{-3}$) and not zero for lower altitudes. To mitigate this error, we only calculated our averages up to the second highest energy bin.

Appendix B PFISR Data

This work uses PFISR data collected in three closely related modes named MSWinds23, MSWinds26, and MSWinds27. All three of these modes interleave three different pulse types optimized for the D-region, E-region, and F-region, respectively, with most of the available duty cycle dedicated to the D-region portion. The D-region portion uses 13-baud Barker codes with 10 μs baud, oversampled at 5 μs, with a 2 ms interpulse period (IPP). The E-region portion uses 16-baud randomized alternating code with 30 s baud, and the F-region portion uses 480 μs uncoded long pulses. Both MSWinds23 and MSWinds26 send 256 consecutive Barker coded pulses in each of the four beam directions and then cycles through the complete set of 32 alternating codes and 32 long pulses on each of the four beam directions. Sending the Barker codes on consecutive pulses allows for the computation of pulse-to-pulse autocorrelation functions and spectra in the D-region, but it has the detrimental effect of introducing range-aliased returns from ranges at integer multiples of 300 km. MSWinds23 transmits the Barker codes and alternating codes on 449.3 MHz and the long pulses on 449.6 MHz. In MSWinds23 the dedicated noise samples on 449.3 MHz are taken by the alternating code channel and need to be rescaled according to the

different filter bandwidth to be applied to the Barker code data. MSWinds26 improves this by transmitting the Barker codes on 449.3 MHz, alternating codes on 449.6 MHz, and long pulses on 449.8 MHz, and incorporating dedicated noise samples on all three channels. MSWinds27 is identical to MSWinds26, except it changes the pulse repetition pattern for the Barker codes. Rather than transmitting 256 pulses on each of the four beams, each cycle MSWinds27 transmits 2048 consecutive pulses on the vertical beam and then 128 consecutive pulses on each of the other three beams. This gives MSWinds27 significantly better statistics on the vertical beam at the expense of reduced statistics on the other positions.

This study uses electron density estimated from the received Barker code power and error estimates for that electron density determined from the number of pulses averaged and the signal-to-noise ratio. In addition to random errors, this electron density estimate is potentially subject to systematic bias if the subtracted noise is too small. PFISR has certain hardware issues that cause the noise to be slightly higher at short ranges than at long ranges. Furthermore, the D-region returns can be corrupted by range-aliased F-region returns. Both of these problems bias the lower D-region electron density estimates high. In order to compensate for this bias, we have assumed the true electron density between 55 and 60 km is always indistinguishable from zero. We estimate the bias by averaging the power between 55 and 60 km and subtracting it off from the power profiles before converting to electron density. This bias can be on the order of an electron density of 10^9 m^{-3}, which is a minor correction to the typical electron densities in pulsating aurora (above 10^{10} m^{-3}). Nonetheless, this bias correction is needed to prevent the inversions

from incorrectly estimating tails of relativistic electrons in order to match the lowest altitude data.

Appendix C Possible Sources of Error

It is worth describing possible sources of systematic error in our results. One, several previous studies found that the energy content becomes harder during the on phase of pulsating aurora (Hosokawa & Ogawa, 2015; Whalen et al., 1971). Our data is integrated over one minute, so these variations will likely be smoothed out, thus reducing the hardness. Two, we are not capturing the full range of the energy flux. Ionization associated with electron energies less than about 1 keV usually peaks above the altitudes that PFISR measures in the D-region mode (Fang et al., 2010). If the energy flux for this portion of the spectrum is significant, we could be overestimating the hardness and underestimating the total energy. Three, the sensitivity of PFISR limits our ability to detect higher energy, lower flux electrons. If populations such as these are present, we could be underestimating the hardness. Four, we only selected pulsating aurora that were in the center of the imager, but we didn't account for times that the PFISR beam wasn't directly on a pulsating patch. If the precipitating flux is highly local, we could be underestimating the energy flux during such periods.

Table S1.

Filename: pa-pfisr-database-table.xlsx

Caption: Table containing the date, start time, and end time of each pulsating aurora event that we analyzed. These were as seen from the Poker Flat Research Range while the

Poker Flat Incoherent Scatter Radar was running during either MSWinds23, MSWinds26, or MSWinds27.

Figure S3.

References

Barrett, J. L., & Hays, P. B. (1976, January). Spatial distribution of energy deposited in nitrogen by electrons. *Journal of Chemical Physics*, *64*(2), 743-750. doi: 10.1063/1.432221

Fang, X., Randall, C. E., Lummerzheim, D., Wang, W., Lu, G., Solomon, S. C., & Frahm, R. A. (2010, November). Parameterization of monoenergetic electron impact ionization. *Geophysical Research Letters*, *37*(22), L22106. doi: 10.1029/2010GL045406

Gledhill, J. A. (1986, June). The effective recombination coefficient of electrons in the ionosphere between 50 and 150 km. *Radio Science*, *21*(3), 399-408. doi: 10.1029/RS021i003p00399

Glukhov, V. S., Pasko, V. P., & Inan, U. S. (1992, November). Relaxation of transient lower ionospheric disturbances caused by lightning-whistler-induced electron precipitation bursts. *Journal of Geophysical Research*, *97*(A11), 16971-16979. doi: 10.1029/92JA01596

Hedin, A. E. (1991, February). Extension of the MSIS thermosphere model into the middle and lower atmosphere. *Journal of Geophysical Research*, *96*(A2), 1159-1172. doi: 10.1029/90JA02125

Hosokawa, K., & Ogawa, Y. (2015, July). Ionospheric variation during pulsating aurora. *Journal of Geophysical Research (Space Physics)*, *120*(7), 5943-5957. doi: 10.1002/

2015JA021401

Kirkwood, S., & Osepian, A. (1995, January). Quantitative Studies of Energetic Particle Precipitation Using Incoherent Scatter Radar. *Journal of Geomagnetism and Geoelectricity*, *47*(8), 783-799. doi: 10.5636/jgg.47.783

Lehtinen, N. G., & Inan, U. S. (2007, April). Possible persistent ionization caused by giant blue jets. *Geophysical Review Letters*, *34*(8), L08804. doi: 10.1029/2006GL029051

Marshall, R. A., Xu, W., Kero, A., Kabirzadeh, R., & Sanchez, E. (2019, February). Atmospheric effects of a relativistic electron beam injected from above: chemistry, electrodynamics, and radio scattering. *Frontiers in Astronomy and Space Sciences*, *6*, 6. doi: 10.3389/fspas.2019.00006

Mitra, A. P. (1981, August). Chemistry of middle atmospheric ionization - a review. *Journal of Atmospheric and Terrestrial Physics*, *43*, 737-752. doi: 10.1016/0021-9169(81)90050-7

Osepian, A., Kirkwood, S., Dalin, P., & Tereschenko, V. (2009, October). D-region electron density and effective recombination coefficients during twilight - experimental data and modelling during solar proton events. *Annales Geophysicae*, *27*(10), 3713-3724. doi: 10.5194/angeo-27-3713-2009

Semeter, J., & Kamalabadi, F. (2005, April). Determination of primary electron spectra from incoherent scatter radar measurements of the auroral E region. *Radio Science*, *40*(2), RS2006. doi: 10.1029/2004RS003042

Sivadas, N., Semeter, J., Nishimura, Y., & Kero, A. (2017, October). Simultaneous Measurements of Substorm-Related Electron Energization in the Ionosphere and the

Plasma Sheet. *Journal of Geophysical Research (Space Physics)*, *122*(10), 10,528-10,547. doi: 10.1002/2017JA023995

Vickrey, J. F., Vondrak, R. R., & Matthews, S. J. (1982, July). Energy deposition by precipitating particles and Joule dissipation in the auroral ionosphere. *Journal of Geophysical Research*, *87*(A7), 5184-5196. doi: 10.1029/JA087iA07p05184

Whalen, B. A., Miller, J. R., & McDiarmid, I. B. (1971, January). Energetic particle measurements in a pulsating aurora. *Journal of Geophysical Research*, *76*(4), 978. doi: 10.1029/JA076i004p00978

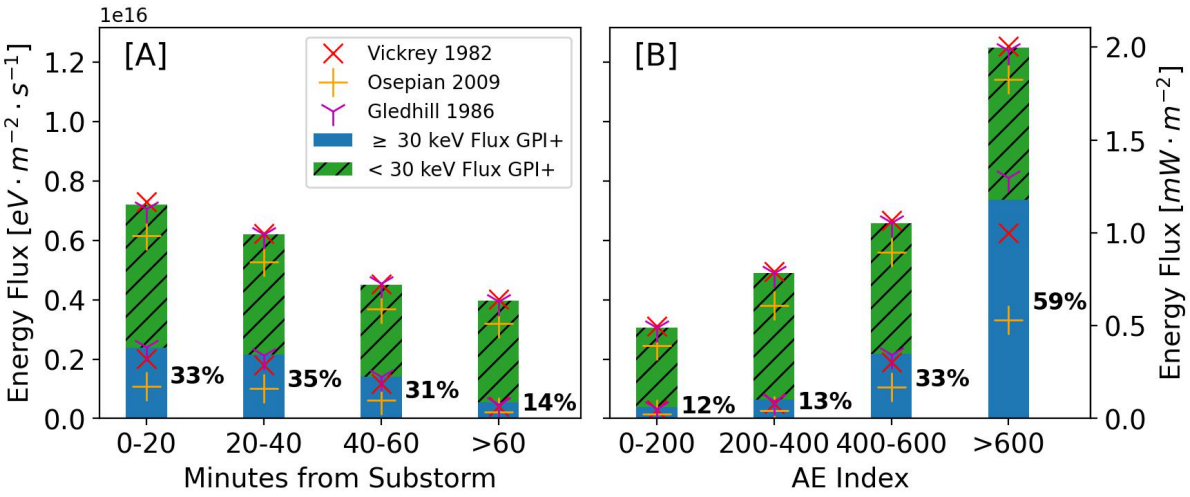

Figure S1. The high ($\geq$ 30 keV) and low ($<$ 30 keV) differential energy flux contributions to pulsating aurora events occurring in four temporal bins relative to substorm onset [A] and AE index [B]. We set the bar heights to the GPI+ model. The scatter points indicate the individual values from the three other chemistry models.

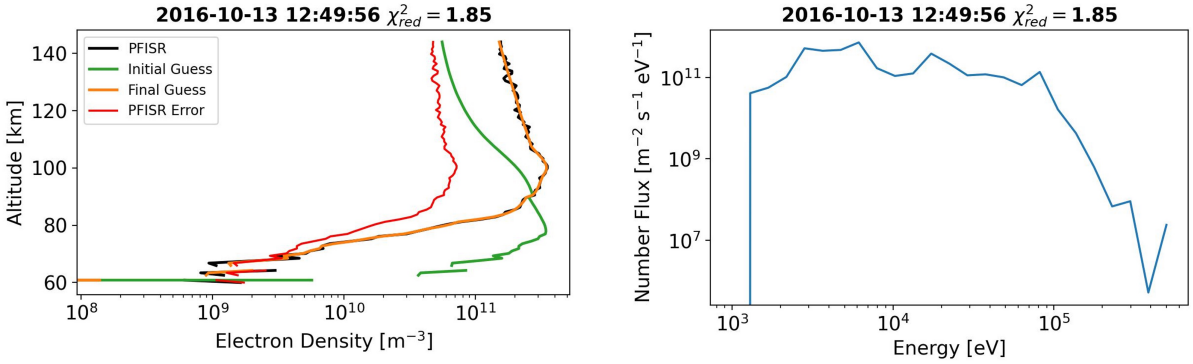

Figure S2. An example fitted electron density using the maximum entropy method along with the GPI+ chemistry model. The plot on the left shows the PFISR measured electron density (black) along with the associated error (red). The initial guess is shown in green and the final fit is shown in orange. The plot on the right is the differential number flux over the range of energies given to the model.

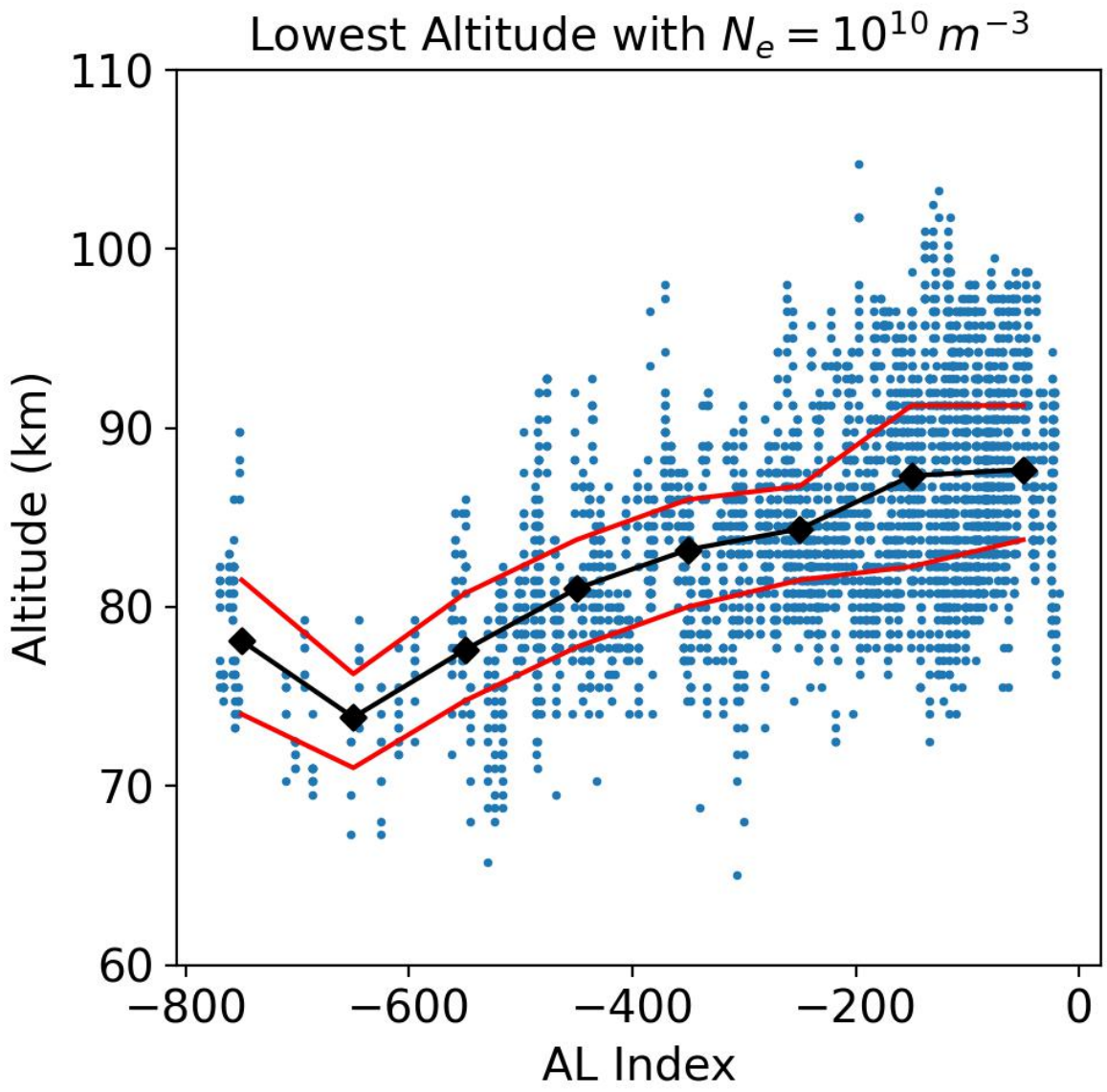

Figure S3. Lowest altitude PFISR measurements during pulsating aurora with $N_e = 10^{10}\,\mathrm{m}^{-3}$ plotted versus AL indices. The black diamonds indicate the average altitude for the surrounding hour, 20 minutes, 200 AE units respectively. The red lines indicate the 25% and 75% quartiles..